



# Polar Circumtriple Planets and Disks Can Only Form Close to a Triple Star

Stephen Lepp<sup>1,2</sup> , Rebecca G. Martin<sup>1,2</sup> , and Stephen H. Lubow<sup>3</sup> <sup>1</sup> Nevada Center for Astrophysics, University of Nevada, Las Vegas, 4505 S. Maryland Parkway, Las Vegas, NV 89154, USA<sup>2</sup> Department of Physics and Astronomy, University of Nevada, Las Vegas, 4505 S. Maryland Parkway, Las Vegas, NV 89154, USA<sup>3</sup> Space Telescope Science Institute, 3700 San Martin Drive, Baltimore, MD 21218, USA

Received 2022 November 1; revised 2022 December 28; accepted 2023 January 2; published 2023 January 23

## Abstract

Observations of protoplanetary disks around binary and triple star systems suggest that misalignments between the orbital plane of the stars and the disks are common. Motivated by recent observations of polar circumbinary disks, we explore the possibility of polar circumtriple disks and therefore polar circumtriple planets that could form in such a disk. With  $n$ -body simulations and analytic methods, we find that the inclusion of a third star, and the associated apsidal precession, significantly reduces the radial range of polar orbits so that circumtriple polar disks and planets can only be found close to the stellar system. Outside of a critical radius that is typically in the range of 3–10 times the outer binary separation, depending upon the binary parameters, the orbits behave the same as they do around a circular orbit binary. For some observed systems that have shorter-period inner binaries, the critical radius is considerably larger. If polar circumtriple planets can form, we suggest that it is likely that they form in a disk that was subject to breaking.

*Unified Astronomy Thesaurus concepts:* [Exoplanet dynamics \(490\)](#); [Celestial mechanics \(211\)](#); [Trinary stars \(1714\)](#); [Protoplanetary disks \(1300\)](#)

## 1. Introduction

Multiple stellar systems are common in star-forming regions (Duchêne & Kraus 2013). Disks around triple star systems are also expected to be common (Tobin et al. 2016; Bate 2018), and there are several well-known examples including GG Tauri A (Di Folco et al. 2014; Keppler et al. 2020; Phuong et al. 2020a) and GW Ori (Bi et al. 2020; Kraus et al. 2020; Smallwood et al. 2021). A common feature of these disks is that they are tilted with respect to the orbital plane of the stars. Disk misalignment may initially occur, for example, because of turbulence in the molecular gas cloud (Offner et al. 2010; Bate 2012; Tokuda et al. 2014) or later accretion of material by the young binary (Bate et al. 2010; Bate 2018). Misalignment may be increased later by stellar flybys (Nealon et al. 2020) or bound stellar companions (e.g., Martin & Lubow 2017; Martin et al. 2022).

Around an eccentric binary star system, test particle orbits have two stable stationary states: coplanar alignment to the binary orbit and polar alignment, in which the angular momentum of the particle orbit is aligned to the binary eccentricity vector and  $90^\circ$  to the binary orbital plane (Verrier & Evans 2009; Farago & Laskar 2010; Doolin & Blundell 2011; Chen et al. 2019). A particle that is misaligned from one of these two stationary states undergoes nodal precession. Low initial inclination orbits precess about the binary angular momentum vector, while high initial inclination orbits precess about the binary eccentricity vector. Since the test particle does not affect the dynamics of the binary, the qualitative behavior does not depend on the orbital radius of the particle around the binary unless general relativity or tides become important (Lepp et al. 2022).

A circumbinary disk with a low mass can undergo similar dynamical behavior to a test particle (e.g., Aly et al. 2015; Martin & Lubow 2018). If the disk is in good radial communication, it can undergo solid body precession at an angular momentum weighted average rate (Papaloizou & Terquem 1995; Larwood et al. 1996). For protoplanetary disks, the radial communication is wavelike (Papaloizou & Pringle 1983; Lubow & Ogilvie 2001). Dissipation in the disk leads to alignment either toward coplanar (Facchini et al. 2013; Nixon et al. 2013) or polar, depending on the initial tilt (Martin & Lubow 2017; Lubow & Martin 2018; Zanazzi & Lai 2018; Cuello & Giuppone 2019). Several polar circumbinary disks around eccentric binaries have been observed (Kennedy et al. 2012, 2019; Kenworthy et al. 2022) although none have yet been observed around a triple star. While polar circumbinary planets have not yet been observed, their formation may be as efficient as in a coplanar configuration (Childs & Martin 2021a, 2021b).

While the evolution of circumbinary particles and disks is now fairly well understood, the inclusion of an inner hierarchical triple star system has not been explored in detail. In this work, for the first time, we examine the effect of an inner triple star system on the existence of polar orbits. In Section 2 we use  $n$ -body simulations, and in Section 3 we compare them to analytic models. The inner and outer binaries that compose the triple star undergo apsidal precession. We show that this can remove the possibility of polar orbits outside of a critical radius from the triple star. This is similar to the effects of general relativity that also causes apsidal precession of the binary (Lepp et al. 2022) but with much higher precession rates. In Section 4 we draw our conclusions and discuss implications both for observations of circumtriple disks and for the properties of planets that may form in such disks.

## 2. Circumtriple Particle Orbits

In this section we first consider the dynamics of a particle orbiting a triple star with our standard parameters, and then we



Original content from this work may be used under the terms of the [Creative Commons Attribution 4.0 licence](#). Any further distribution of this work must maintain attribution to the author(s) and the title of the work, journal citation and DOI.

consider the effect of varying different triple star parameters. We use the REBOUND  $N$ -body code (Rein & Liu 2012). The simulations were integrated using a combination of IAS15, a 15th order Gauss–Radau integrator (Rein & Spiegel 2015) and the WHFast, a symplectic Wisdom–Holman integrator (Wisdom & Holman 1991; Rein & Tamayo 2015).

### 2.1. Triple Star Parameters

Triple star systems are found to occur with a large range of properties. Figure 3 of Tokovinin (2021) plots the outer binary period as a function of the inner binary period for a sample of 1820 systems that lie within a distance of 200 pc. The sample is subject to strong selection effects that favor the detection of close spectroscopic binaries and resolved wide binaries. Nonetheless, the plot suggests that for longer-period inner binaries ( $>1y$ ), the outer to inner semimajor axis ratios typically range from 3 to 50. For shorter-period inner binaries ( $<1y$ ), the ratio range is typically from 20 to 100, and ratios of greater than 1000 also occur.

Triple star systems may be unstable for a wide range of parameter space (Mardling & Aarseth 2001; Valtonen & Karttunen 2006; Vynatheya et al. 2022). We consider hierarchical triple systems composed of an inner binary with an outer binary companion. The inclination of the inner binary to the inclination of the binary companion must be small enough to avoid von Zeipel–Kozai–Lidov (ZKL) oscillations (von Zeipel 1910; Kozai 1962; Lidov 1962; Naoz 2016; Hamers 2021). Figure 3 of Tokovinin (2021) shows evidence of the stability limit at a period ratio of about 4.7 predicted by Mardling & Aarseth (2001). For the range of parameters studied, the eccentricity of all the particle orbits are relatively constant.

The orbits are scale free in mass and length, and we adopt as our mass unit the total mass of the triple star system,  $m_{AB}$ , and for our length unit, the semimajor axis of the outer companion,  $a_{AB}$ . For our standard parameters, the inner binary has a total mass  $m_A$  and is composed of an equal mass binary with  $m_{Aa} = m_{Ab} = 0.25 m_{AB}$ , semimajor axis  $a_A = a_{AB}/20$ , eccentricity  $e_A = 0$ , and an inclination of  $i_A = 0$  (coplanar) relative to outer companions orbit. The outer companion to the binary has mass  $m_B = m_A = 0.5 m_{AB}$  and is in an orbit with an eccentricity of  $e_{AB} = 0.5$ .

More generally, we define the relative mass of the inner binary as  $f_A = \frac{m_{Ab}}{m_{Aa} + m_{Ab}}$ , where  $m_{Ab}$  is the smaller of the two masses, and so this parameter ranges from 0 to 0.5. The relative mass of the companion is  $f_B = \frac{m_B}{m_{AB}}$ . Since the companion may be smaller or larger in mass than the inner binary, this parameter ranges from 0 to 1. Our standard parameters have  $f_A = 0.5$  and  $f_B = 0.5$ . These parameters are in the stable region for circumtriple systems. The system becomes unstable with larger  $a_A$  and  $e_{AB}$ . Adopting the multilayer perceptron (MLP) model from Vynatheya et al. (2022) and varying  $e_{AB}$ , we find it is stable for  $e_{AB} \lesssim 0.8$  and  $a_A/a_{AB} \lesssim 0.13$ . We check our ranges of parameters with the MLP model (Vynatheya et al. 2022) to avoid unstable regions. However, the transition between stable and unstable is gradual rather than abrupt (Hayashi et al. 2022), and so we have chosen our standard parameters to be well clear of unstable regions.

### 2.2. Test Particle Orbits around Our Standard Triple Star

We run test particle orbits at radius  $r$  around the triple star. The test particles can have unstable orbits if they are too close to the AB binary (Holman & Wiegert 1999; Chen et al. 2020; Quarles et al. 2020). We only consider orbits at radii large enough to be stable. We analyze the test particle orbits in the frame of the AB binary made up of the companion star orbiting the inner binary. We characterize the test particle orbit by its inclination and nodal phase angle relative to this binary. The inclination of the orbit is given by

$$i = \cos^{-1}(\hat{l}_{AB} \cdot \hat{l}_p), \quad (1)$$

where  $\hat{l}_{AB}$  is a unit vector in the direction of the AB binary angular momentum and  $\hat{l}_p$  is a unit vector in the direction of the particle’s angular momentum. The nodal phase angle is the angle measured relative to the eccentricity vector of the outer binary and is given by

$$\phi = \tan^{-1} \left( \frac{\hat{l}_p \cdot (\hat{l}_{AB} \times \hat{e}_{AB})}{\hat{l}_p \cdot \hat{e}_{AB}} \right) + 90^\circ, \quad (2)$$

(Chen et al. 2019, 2020) where  $\phi$  is the phase angle and  $\hat{e}_{AB}$  is the eccentricity vector of the outer binary.

We run test particle orbits around our standard triple star that begin in circular orbits at radii of  $r = 3.5, 4.5, 5.5,$  and  $6 a_{AB}$ . We start with initial inclinations in  $10^\circ$  increments from  $10^\circ$  to  $170^\circ$  and with an initial longitude of the ascending node of  $90^\circ$ . The resulting orbits are plotted in the  $(i \cos \phi, i \sin \phi)$  phase plane in the left panel of Figure 1. The right panel shows the same information but displays the paths of the particle’s orbital angular momentum vector on the unit sphere.

For low initial inclinations, there is a circulating region shown in green, in which the particle angular momentum vector precesses around the binary angular momentum vector. The retrograde circulation region is shown in blue where the particle’s angular momentum vector is orbiting about the negative of the binary’s angular momentum vector. There is a librating region, shown in red, where the particle angular momentum vector precesses around a stationary inclination. This stationary inclination for close-in particles is at  $i = 90^\circ$  and aligned with the binary eccentricity vector. As the particle moves to larger orbital radii, the stationary inclination moves to higher inclinations. Once the stationary inclination is  $>180^\circ$ , there are no more librating orbits, and the particle has similar dynamics to one around a circular orbit binary since it nodally precesses about the binary angular momentum vector for all inclinations. This is very similar to the behavior seen in Lepp et al. (2022) where we considered test particle orbits about a binary that was precessing due to the effects of general relativity. Here the behavior of the triple star system is causing a similar precession but at a timescale over an order of magnitude higher.

All the simulations in this paper were run with zero-mass test particles, but to see the effects of a massive particle, we ran select simulations with various mass particles. The simulations are essentially unchanged by introducing a particle up to  $m_{AB}/1000$  (about a Jupiter mass if  $m_{AB} \approx 1 M_\odot$ ). A Jupiter mass particle follows the test particle evolution. Masses significantly above this mass can change the evolution. In

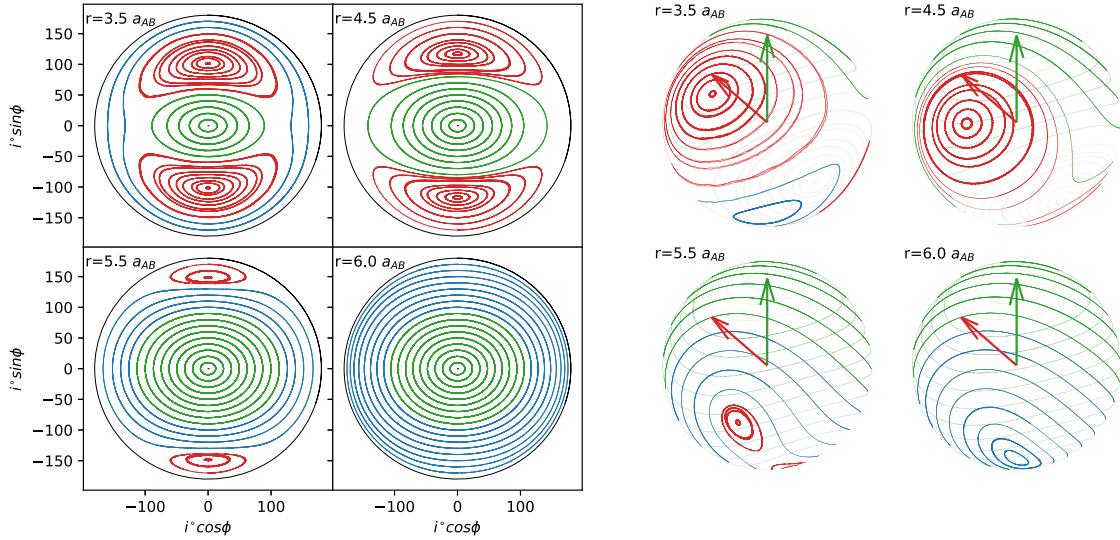


**Figure 1.** Test particle orbits around our standard triple star at orbital radii of  $r = 3.5, 4.5, 5.5,$  and  $6 a_{AB}$ . Left: the  $(i \cos \phi, i \sin \phi)$  phase plane. Right: precession paths for the angular momentum vector of the test particles plotted on surface of sphere. The angular momentum and eccentricity unit vectors are shown in green and red, respectively. The circulating orbits are shown in green, librating orbits are red, and retrograde circulating orbits are blue.

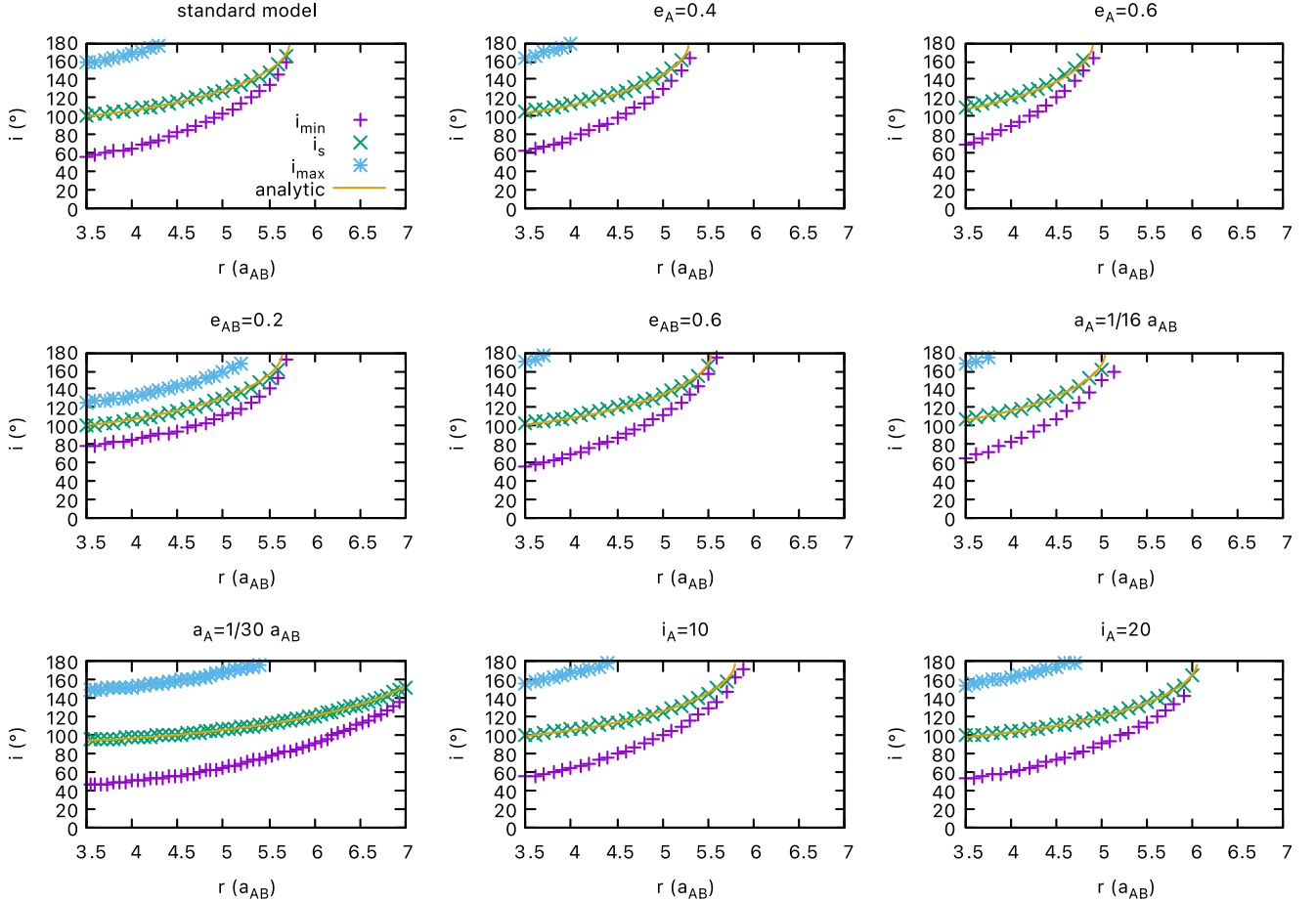


**Figure 2.** The minimum initial inclination ( $i_{\min}$ , magenta), maximum initial inclination ( $i_{\max}$ , blue) for librating orbits, and the stationary polar inclination (green) for varying  $e_A, e_{AB}, a_{AB}$ , or  $i_A$  (in degrees) from our standard model. The analytic curve for the stationary state is from Equation (8), with  $\alpha = 2$ . The key in upper left panel applies to all nine panels.

particular, large masses in polar orbits induce a precession in the outer binary in the opposite direction of that caused by the inner binary and cause the total precession of the outer binary to be slower.

### 2.3. Critical Radius for Librating Orbits

In Figure 2 we show the smallest initial inclination for a librating orbit,  $i_{\min}$ ; the largest initial inclination for a librating orbit,  $i_{\max}$ ; and the stationary inclination,  $i_s$ , where the orbit

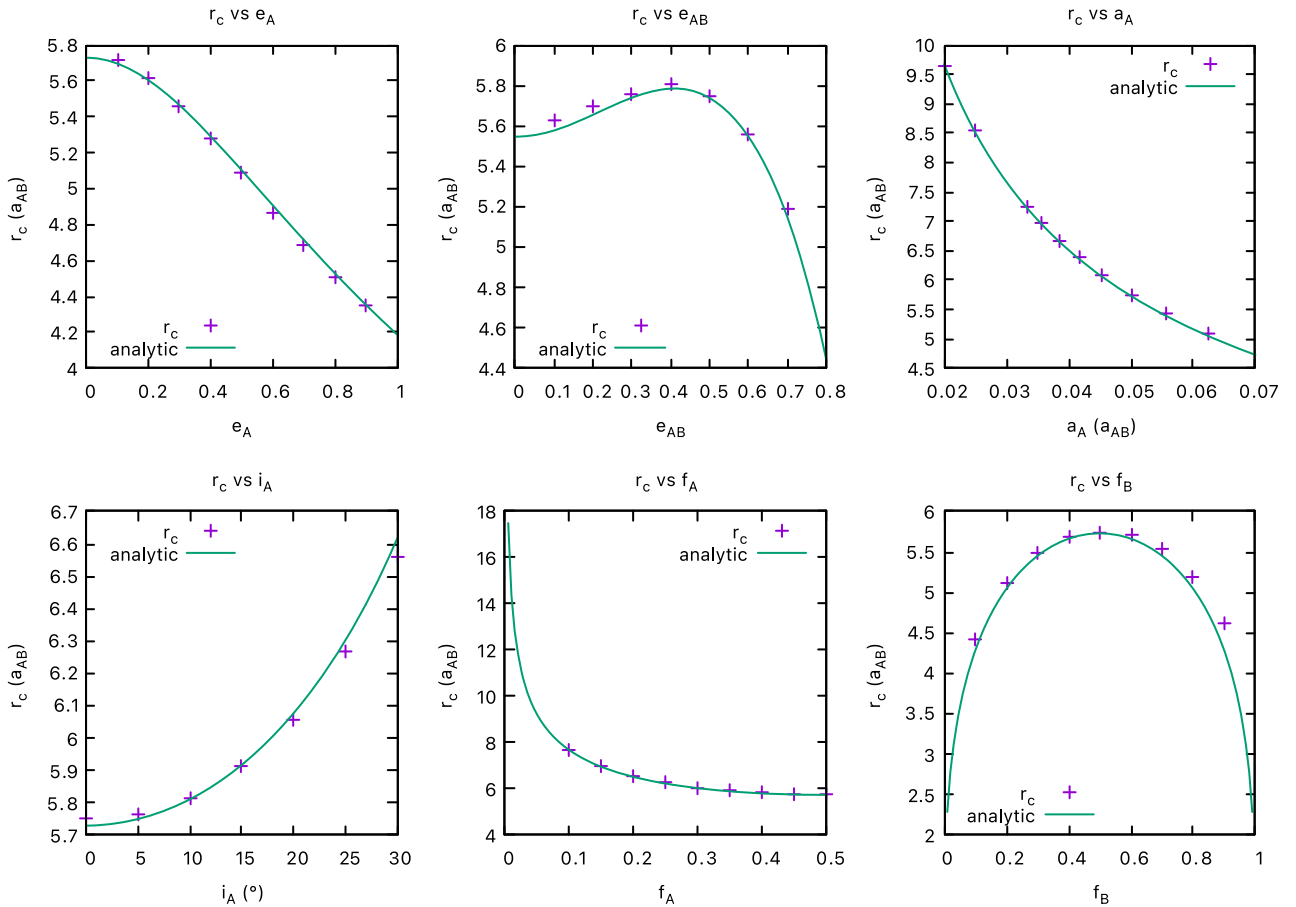


**Figure 3.** The critical radius,  $r_c$ , inside of which there are polar orbits for varying  $e_A$ ,  $e_{AB}$ ,  $a_A$ ,  $i_A$ ,  $f_A$ , and  $f_B$  from our standard model parameters. The purple crosses show numerical simulations, and the green curves show the analytical estimate. The analytic lines only depend on  $\alpha$  in the top left panel (since  $e_A = 0$  everywhere else), and there we take  $\alpha = 2$ .

stays at a fixed inclination with no nodal precession. The upper left panel in Figure 2 represents our standard triple star parameters. There are circulating orbits at low inclinations  $i < i_{\min}$  and retrograde circulating orbits for  $i > i_{\max}$ . If  $i_{\max} > 180^\circ$ , then there is no retrograde circulating region and since the librating orbits occur around  $i_s$ , there are no librating orbits when  $i_s > 180^\circ$ . The precession of the triple star system causes the stationary inclination to move to higher inclinations with increasing test particle radius, until it becomes greater than  $180^\circ$ , and then there are no librating orbits. We call this radius the critical radius,  $r_c$ , and it represents the maximum radius at which test particles can orbit the outer binary in a polar orbit. For our standard triple star parameters,  $r_c = 5.7 a_{AB}$ .

We now consider the effect of varying the triple star orbital parameters on the test particle orbits. The other panels in Figure 2 take our standard model and vary one of the parameters. In the next two panels across the top, we vary the eccentricity of the inner binary from  $e_A = 0$  to  $e_A = 0.4$  and  $e_A = 0.6$ . The change in  $e_A$  increases the apsidal precession rate of the AB binary by about 30% for  $e_A = 0.4$  and about 70% for 0.6. The radius  $r_c$  then occurs at smaller orbital radii of  $5.28$  and  $4.87 a_{AB}$  for  $e_A = 0.4$  and  $e_A = 0.6$ , respectively.

Next, we vary from our standard case the eccentricity of the companion from its value of  $e_{AB} = 0.5$  to  $e_{AB} = 0.2$  and  $e_{AB} = 0.6$ . In both cases,  $r_c$  is reduced though the effect is much weaker than that seen for varying  $e_A$ . This is because  $e_{AB}$  affects both the precession rate of the ascending node of the test

particle and the apsidal precession rate of the AB binary (see Section 3).

We then vary the ratio of the semimajor axis of the inner binary to the companion from its standard value of  $a_A/a_{AB} = 1/20$ . For  $a_A/a_{AB} = 1/16$  we find  $r_c \approx 5 a_{AB}$ , and for  $a_A/a_{AB} = 1/30$ , we find  $r_c = 7.25 a_{AB}$ , which is off the range of the plot. This again reflects the change in the apsidal precession rate of the binary with changing geometry. Finally, we consider the effect of the inclination of the inner binary relative to the triple star companion. We have restricted our simulations to small angle inclinations to avoid ZKL oscillations that would introduce additional time variations. We change our standard model to have the inner binary’s orbit inclined to the orbital plane of the companion, and this increases  $r_c$ . The critical radius gets larger as the apsidal precession rate gets smaller. However, we note that the inclination has a weak effect on the critical radius.

Figure 3 shows the critical radius  $r_c$  as a function of some of the triple star parameters. The crosses show the numerical determination of the radius. We vary  $e_A$ ,  $e_{AB}$ ,  $a_A$ ,  $i_A$ ,  $f_A$ , and  $f_B$ . The critical radius depends on the rate of the apsidal precession of the AB binary as well as on the nodal precession rate of the test particle orbit (see the next section). The faster the apsidal precession, the smaller the critical radius. For typical triple star parameters (Tokovinin 2008, 2021), the critical radius is in the approximate range  $3 - 10 a_{AB}$ , unless one of the stars has a much smaller mass than the others. The innermost stable orbit for a polar circumbinary test particle is typically around



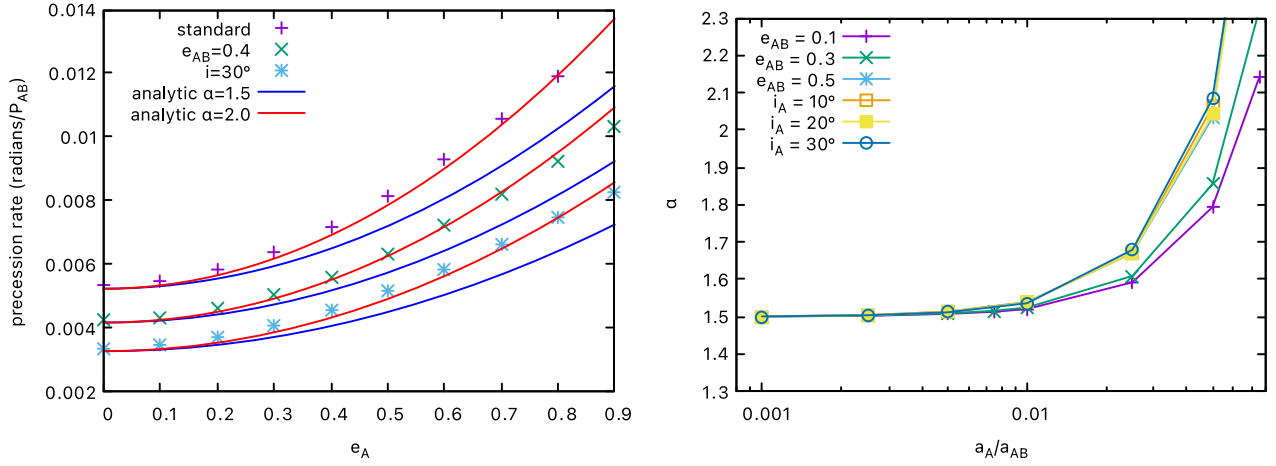


**Figure 4.** Left: apsidal precession rate ( $\dot{\omega}$ ) variation with  $e_A$  around our standard triple star, one with  $e_{AB} = 0.4$ , and one with an inclination  $i_A = 30^\circ$ . The analytical fits are shown with coefficients of both  $\alpha = 1.5$  and  $\alpha = 2.0$ . Right: the coefficient  $\alpha$  in front of  $e_A^2$  in the precession formula averaged over the values of  $e_A$  from 0.1 to 0.9.

$2 - 2.5 a_{AB}$  (Chen et al. 2020), and so the radial range of stable polar circumtriple orbits may be quite small. However, as discussed in Section 2.1, some observed triple star systems found with short-period inner binaries have more extreme outer to inner semimajor axis ratios that allow the critical radius to extend to more than  $80 a_{AB}$ .

The libration timescale increases with the semimajor axis of the test particle. For our standard model, the critical radius outside of which there are no polar orbits is  $r_c = 5.73 a_{AB}$ . In this case, for a test particle at  $r = 5.5 a_{AB}$ , orbits near the stationary inclination librate about it with a period of about  $4000 P_{AB}$ , where  $P_{AB}$  is the orbital period of the outer binary. At an orbital radius of  $r = 4.5 a_{AB}$ , orbits near the stationary inclination librate with a period of about  $800 P_{AB}$ .

### 3. Analytical Estimation

The stationary inclination occurs where the apsidal precession rate of the binary is equal to the nodal precession rate of the test particle. We follow Zanardi et al. (2018) to analytically find the stationary inclination based on the quadrupole order expansion of the Hamiltonian. They derived it for the case where general relativity drives the apsidal precession. The precession of the ascending node of the test particle is given by Equation (4) in Zanardi et al. (2018). For a circular ( $e = 0$ ) polar stationary orbit ( $\Omega = 90^\circ$ ), the nodal precession rate is

$$\dot{\Omega}_s = -\frac{m_A m_B k}{m_{AB}^{3/2} r^{3/2}} \left( \frac{a_{AB}}{r} \right)^2 \frac{3 \cos i (1 + 4e_{AB}^2)}{4}, \quad (3)$$

where  $k^2$  is the gravitational constant. We equate this to the rate of change of the longitude of the periapsis for the binary,  $\dot{\omega}_{AB} = \dot{\omega}_A + \dot{\Omega}_{AB}$ , to find the stationary inclination for the test particle:

$$i_s = \cos^{-1} \left( -\frac{\dot{\omega}_{AB}}{3k} \frac{4 (m_{AB})^{3/2} r^{7/2}}{m_A m_B} \frac{1}{a_{AB}^2 (1 + 4e_{AB}^2)} \right). \quad (4)$$

This formula is general, and the apsidal precession rate for the binary could come from general relativity (e.g., Zanardi et al. 2018), tidal interactions (e.g., Sterne 1939), or interactions with a companion star (e.g., Morais & Correia 2012).

The precession rate of the longitude of the periapsis of the companion in a triple in the quadrupole approximation is given by

$$\dot{\omega}_{AB} = \left( \frac{3k}{4} \right) \left( \frac{m_{Aa} m_{Ab} (m_{AB})^{1/2}}{(m_A)^2} \right) \times \left( \frac{a_A^2}{a_{AB}^{7/2}} \right) \left( \frac{1}{(1 - e_{AB}^2)^2} \right) F(e_A, i_A), \quad (5)$$

where

$$F(e_A, i_A) = (1 + \alpha e_A^2) \left( \frac{3 \cos(i_A)^2 - 1}{2} \right) + \frac{15}{4} e_A^2 (1 - \cos(i_A)^2) \cos(2\omega_A) \quad (6)$$

(see Equations (25) and (26) in Morais & Correia 2012), where  $i_A$  is the inclination of the inner binary relative to the outer binary, and  $\omega_A$  is the argument of the periapsis of the inner binary measured relative to the outer binary. The same rate may also be found for the coplanar case by adding all the quadrupole terms for  $\dot{\omega}$  and  $\dot{\Omega}$  for the outer binary (Equations (74) and (76) in Naoz 2016); the inclination dependence is slightly different as Morais & Correia (2012) approximate the outer binary as the fixed plane. In all our configurations, the outer binary carries most of the angular momentum, and so this is a good approximation, as seen in Figures 2–4. The first term in Equation (6) sets the average rate of apsidal precession, and the second term causes an oscillation about this average precession rate. If  $\omega_A$  is an odd multiple of  $45^\circ$ , then the second term is zero. In practice, one can ignore the second term if one wants the average precession over long times or in a time that is centered around an odd multiple of  $45^\circ$ . The expression is valid so long as  $a_A \ll a_{AB}$  and  $m_B$  is not much less than  $m_A$ , meaning that the AB binary has most of the angular momentum, and thus the AB binary plane is very nearly a fixed plane in the system.

For an inclination of zero, the function in Equation (6) simplifies to

$$F(e_{AB}, 0) = (1 + \alpha e_A^2). \quad (7)$$

Here, the  $\alpha = \frac{3}{2}$  factor given in Morais & Correia (2012) works well in the limit of  $a_{AB} \gg a_A$ , and we find it works well for ratios of  $a_A/a_{AB} \lesssim 0.005$ . However, our standard triple star has  $a_A/a_{AB} = 0.05$ , and so higher order terms have changed this parameter. In Naoz (2016) it is clear that the octupole terms vanish for our standard case of an equal mass inner binary, and so it must be due to even higher order terms (e.g., Yokoyama et al. 2003; Vinson & Chiang 2018; de Elía et al. 2019). We now consider numerical fits for this parameter.

The left panel of Figure 4 shows the numerically determined particle precession rates around the triple star as a function of  $e_A$ . We consider the standard model with  $e_{AB} = 0.4$  and the standard model with  $i_A = 30^\circ$ . To get an accurate precession rate, we average the precession rate over 40 periods of the AB binary and over a time with the relative angle of the precession of  $45^\circ$ ; this assures that the second term in Equation (6) averages to zero.

In the right-hand panel, we show a numerical determination of  $\alpha$  as a function of  $a_A/a_{AB}$ . We take  $e_{AB} = 0.1, 0.3,$  and  $0.5$  with a coplanar binary and inclinations of  $10^\circ, 20^\circ,$  and  $30^\circ$  with  $e_{AB} = 0.5$ . For each point, we vary  $e_A$  between 0.1 and 0.9 in steps of 0.1 and find for each an exact  $\alpha$  that would give that rate relative to the  $e_A = 0$  rate. We then average all of these. At small ratios of  $a_A/a_{AB}$ , the best fit for  $\alpha$  is  $3/2$ , but close to our standard model  $a_A/a_{AB} = 0.05$ , a much better fit is  $\alpha = 2$ .

We now take  $\tilde{\omega}_{AB}$  from Equation (5) and find the stationary inclination with Equation (4) to be

$$i_s = \cos^{-1} \left( -\frac{m_{Aa} m_{Ab} m_{AB}^2}{m_A^3 m_B} \left( \frac{r}{a_{AB}} \right)^{7/2} \times \left( \frac{a_A}{a_{AB}} \right)^2 \frac{1}{(1 + 4e_{AB}^2)(1 - e_{AB}^2)^2} F_e(e_A, i_A) \right). \quad (8)$$

The orange curves in Figure 2 show the analytic stationary inclination with  $\alpha = 2$ . There is good agreement between this and the numerical solutions.

We find the critical particle orbital radius outside of which there are no polar orbits by setting  $i_s = 180^\circ$  and solving for  $r$  to find

$$\frac{r_c}{a_{AB}} = \left( \frac{m_A^3 m_B}{m_{Aa} m_{Ab} m_{AB}^2} \left( \frac{a_{AB}}{a_A} \right)^2 \times \frac{(1 - e_{AB}^2)^2 (1 + 4e_{AB}^2)^{2/7}}{F_c(e_A, i)} \right)^{2/7}. \quad (9)$$

Our standard parameters have  $r_c/a_{AB} = 5.73$ , in agreement with the top left panel of Figure 2. More generally we find

$$\frac{r_c}{a_{AB}} = 5.73 \frac{M A E}{F^{2/7}}, \quad (10)$$

where  $M, A,$  and  $E$  are scaling functions for the radius in terms of mass, semimajor axis, and eccentricity of the companion, which have been normalized to one for our standard

parameters. The scaling with masses is

$$M(m_{Aa}, m_{Ab}, m_B) = \left( \frac{m_A^3 m_B}{m_{Aa} m_{Ab} m_{AB}^2} \right)^{2/7} \quad (11)$$

$$= \left( \frac{(1 - f_B) f_B}{(1 - f_A) f_A} \right)^{2/7}, \quad (12)$$

with semimajor axis is

$$A(a_A, a_{AB}) = \left( \frac{a_{AB}}{20 a_A} \right)^{4/7}, \quad (13)$$

and with the companion eccentricity is

$$E(e_{AB}) = \left( \frac{8(1 - e_{AB}^2)^2 (1 + 4e_{AB}^2)^{2/7}}{9} \right)^{2/7}. \quad (14)$$

The green curves in Figure 3 show this analytic solution for the critical radius. We see that there is good agreement between the numerical and analytic solutions.

#### 4. Discussion and Conclusions

Misaligned circumbinary test particle orbits around an eccentric binary undergo nodal precession either about the binary angular momentum vector ( $i = 0^\circ$ ) or about the stationary polar inclination that is aligned to the binary eccentricity vector ( $i = 90^\circ$ ). The orbit type depends on the initial particle inclination and the binary eccentricity, but it does not depend upon the particle semimajor axis. With  $n$ -body simulations and analytic methods, we have investigated the dynamics of circumtriple particle orbits. For close-in particles, the polar inclination is  $90^\circ$ , and the orbits around the triple star are similar to those around the outer binary, with the inner binary replaced by a single star. However, with a hierarchical triple star, the inner and outer binaries undergo apsidal precession, and this leads to an increasing polar stationary inclination with increasing particle semimajor axis. There is a critical radius  $r_c$  outside of which there are no polar orbits, only circulating orbits that precess about the binary angular momentum vector. We find for typical parameters that the critical radius is in the approximate range 3–10 times the outer binary semimajor axis. Therefore, polar circumtriple orbits typically exist only relatively close to a triple star. But for some observed shorter-period inner binaries ( $< 1y$ ), the ratio of the outer to inner semimajor axis is quite large (Tokovinin 2021). In such cases, the circumtriple orbits can occur at relatively large distances from the outer binary.

A low-mass circumtriple disk can undergo similar behavior to the particles, but the radii of the disk communicate with each other, allowing solid body precession. Therefore, a disk with an outer radius larger than  $r_c$  could reach a polar state. However, because  $r_c$  can be only a few times larger than the outer binary separation, even if a disk began with an outer radius smaller than  $r_c$ , it may quickly spread out beyond this, depending upon the disk viscosity. This suggests that a polar circumtriple disk could form although it may be the inner part of a broken disk. If  $r_c$  is small, communication through the disk may instead lead the outer parts to dominate the behavior and the disk to move toward coplanar alignment. These effects should be investigated in future work.




There are two triple star systems that may have planets orbiting them, GG Tauri A (Phuong et al. 2020b) and GW Ori

(Bi et al. 2020; Smallwood et al. 2021). The GG Tauri A system consists of three stars (Di Folco et al. 2014) with  $m_B = 0.6 M_\odot$ ,  $m_{Aa} = 0.38 M_\odot$ , and  $m_{Ab} = 0.3 M_\odot$ . The outer binary semimajor axis is estimated to be  $a_{AB} = 36$  au and inner binary semimajor axis is about  $a_A = 5.1$  au. The other orbital parameters are uncertain, but we can estimate  $M \approx 1$ ,  $A \approx 0.55$ , and  $r_c = 3.2 a_{AB} = 113$  au. The disk around the triple star system extends from  $r = 180$  au  $\approx 5 a_{AB}$  to 800 au, and the proposed planet is at about 230 au. The second system, GW Ori, has the triple star parameters  $m_{Aa} = 2.47 M_\odot$ ,  $m_{Ab} = 1.43 M_\odot$ ,  $m_{AB} = 1.36 M_\odot$ ,  $a_A = 1.2$  au,  $a_{AB} = 8.89$  au,  $e_A = 0.069$ , and  $e_{AB} = 0.379$  (Kraus et al. 2020). These give  $A = 0.56$ ,  $M = 0.95$ ,  $F = 1$ , and  $E = 1.05$ , and we find  $r_c = 3.0 a_{AB} = 28.4$  au. The observed disk is at  $r > 36$  au  $\approx 4 a_{AB}$ , and the proposed planet is at  $r = 100$  au. Again the disk and the planet are well outside the critical radius.

For both of these observed circumtriple systems, the inner edge of the disk and the orbits of the potential planets are larger than  $r_c$ . This suggests that the dynamics of the planet and disk is similar to that around a circular orbit binary. A coplanar circumbinary disk is truncated at 2–3 times the binary separation (Artymowicz & Lubow 1994), and the cavity size decreases with increasing tilt of the disk (Miranda & Lai 2015; Lubow & Martin 2018; Franchini et al. 2019). Therefore, the inner truncation radius of both of these disks is larger than would be predicted for a circumbinary disk. This could be a result of the triple star effects described in this work that limit the disk to be in  $r > r_c$ . The tidal truncation of a misaligned circumtriple disk should be investigated in future work.

We thank an anonymous referee for useful comments that improved the manuscript. We acknowledge support from NASA through grants 80NSSC21K0395 and 80NSSC19K0443. S.H.L. thanks the Institute for Advanced Study for visitor support.

### ORCID iDs

Stephen Lepp  <https://orcid.org/0000-0003-2270-1310>  
 Rebecca G. Martin  <https://orcid.org/0000-0003-2401-7168>  
 Stephen H. Lubow  <https://orcid.org/0000-0002-4636-7348>

### References

- Aly, H., Dehnen, W., Nixon, C., & King, A. 2015, *MNRAS*, 449, 65  
 Artymowicz, P., & Lubow, S. H. 1994, *ApJ*, 421, 651  
 Bate, M. R. 2012, *MNRAS*, 419, 3115  
 Bate, M. R. 2018, *MNRAS*, 475, 5618  
 Bate, M. R., Lodato, G., & Pringle, J. E. 2010, *MNRAS*, 401, 1505  
 Bi, J., van der Marel, N., Dong, R., et al. 2020, *ApJL*, 895, L18  
 Chen, C., Franchini, A., Lubow, S. H., & Martin, R. G. 2019, *MNRAS*, 490, 5634  
 Chen, C., Franchini, A., Lubow, S. H., & Martin, R. G. 2020, *MNRAS*, 495, 141  
 Chen, C., Lubow, S. H., & Martin, R. G. 2020, *MNRAS*, 494, 4645  
 Childs, A. C., & Martin, R. G. 2021a, *MNRAS*, 507, 3461  
 Childs, A. C., & Martin, R. G. 2021b, *ApJL*, 920, L8  
 Cuellar, N., & Giuppone, C. A. 2019, *A&A*, 628, A119  
 de Elía, G. C., Zanardi, M., Dugaro, A., & Naoz, S. 2019, *A&A*, 627, A17  
 Di Folco, E., Dutrey, A., Le Bouquin, J. B., et al. 2014, *A&A*, 565, L2  
 Doolin, S., & Blundell, K. M. 2011, *MNRAS*, 418, 2656  
 Duchêne, G., & Kraus, A. 2013, *ARA&A*, 51, 269  
 Facchini, S., Lodato, G., & Price, D. J. 2013, *MNRAS*, 433, 2142  
 Farago, F., & Laskar, J. 2010, *MNRAS*, 401, 1189  
 Franchini, A., Lubow, S. H., & Martin, R. G. 2019, *ApJL*, 880, L18  
 Hamers, A. S. 2021, *MNRAS*, 500, 3481  
 Hayashi, T., Trani, A. A., & Suto, Y. 2022, arXiv:2209.08487  
 Holman, M. J., & Wiegert, P. A. 1999, *AJ*, 117, 621  
 Kennedy, G. M., Matrà, L., Facchini, S., et al. 2019, *NatAs*, 3, 230  
 Kennedy, G. M., Wyatt, M. C., Sibthorpe, B., et al. 2012, *MNRAS*, 421, 2264  
 Kenworthy, M. A., González Picos, D., Elizondo, E., et al. 2022, *A&A*, 666, A61  
 Keppler, M., Penzlin, A., Benisty, M., et al. 2020, *A&A*, 639, A62  
 Kozai, Y. 1962, *AJ*, 67, 591  
 Kraus, S., Kreplin, A., Young, A. K., et al. 2020, *Sci*, 369, 1233  
 Larwood, J. D., Nelson, R. P., Papaloizou, J. C. B., & Terquem, C. 1996, *MNRAS*, 282, 597  
 Lepp, S., Martin, R. G., & Childs, A. C. 2022, *ApJL*, 929, L5  
 Lidov, M. L. 1962, *P&SS*, 9, 719  
 Lubow, S. H., & Martin, R. G. 2018, *MNRAS*, 473, 3733  
 Lubow, S. H., & Ogilvie, G. I. 2001, *ApJ*, 560, 997  
 Mardling, R. A., & Aarseth, S. J. 2001, *MNRAS*, 321, 398  
 Martin, R. G., Lepp, S., Lubow, S. H., et al. 2022, *ApJL*, 927, L26  
 Martin, R. G., & Lubow, S. H. 2017, *ApJL*, 835, L28  
 Martin, R. G., & Lubow, S. H. 2018, *MNRAS*, 479, 1297  
 Miranda, R., & Lai, D. 2015, *MNRAS*, 452, 2396  
 Morais, M. H. M., & Correia, A. C. M. 2012, *MNRAS*, 419, 3447  
 Naoz, S. 2016, *ARA&A*, 54, 441  
 Nealon, R., Cuellar, N., & Alexander, R. 2020, *MNRAS*, 491, 4108  
 Nixon, C., King, A., & Price, D. 2013, *MNRAS*, 434, 1946  
 Offner, S. S. R., Kratter, K. M., Matzner, C. D., Krumholz, M. R., & Klein, R. I. 2010, *ApJ*, 725, 1485  
 Papaloizou, J. C. B., & Pringle, J. E. 1983, *MNRAS*, 202, 1181  
 Papaloizou, J. C. B., & Terquem, C. 1995, *MNRAS*, 274, 987  
 Phuong, N. T., Dutrey, A., Diep, P. N., et al. 2020a, *A&A*, 635, A12  
 Phuong, N. T., Dutrey, A., Di Folco, E., et al. 2020b, *A&A*, 635, L9  
 Quarles, B., Li, G., Kostov, V., & Haghighipour, N. 2020, *AJ*, 159, 80  
 Rein, H., & Liu, S.-F. 2012, *A&A*, 537, A128  
 Rein, H., & Spiegel, D. S. 2015, *MNRAS*, 446, 1424  
 Rein, H., & Tamayo, D. 2015, *MNRAS*, 452, 376  
 Smallwood, J. L., Nealon, R., Chen, C., et al. 2021, *MNRAS*, 508, 392  
 Sterne, T. E. 1939, *MNRAS*, 99, 451  
 Tobin, J. J., Looney, L. W., Li, Z.-Y., et al. 2016, *ApJ*, 818, 73  
 Tokovinin, A. 2008, *MNRAS*, 389, 925  
 Tokovinin, A. 2021, *Univ*, 7, 352  
 Tokuda, K., Onishi, T., Saigo, K., et al. 2014, *ApJL*, 789, L4  
 Valtonen, M., & Karttunen, H. 2006, *The Three-Body Problem* (Cambridge: Cambridge Univ. Press)  
 Verrier, P. E., & Evans, N. W. 2009, *MNRAS*, 394, 1721  
 Vinson, B. R., & Chiang, E. 2018, *MNRAS*, 474, 4855  
 von Zeipel, H. 1910, *AN*, 183, 345  
 Vynatheya, P., Hamers, A. S., Mardling, R. A., & Bellinger, E. P. 2022, arXiv:2207.03151  
 Wisdom, J., & Holman, M. 1991, *AJ*, 102, 1528  
 Yokoyama, T., Santos, M. T., Cardin, G., & Winter, O. C. 2003, *A&A*, 401, 763  
 Zanardi, M., de Elía, G. C., Di Sisto, R. P., & Naoz, S. 2018, *A&A*, 615, A21  
 Zanazzi, J. J., & Lai, D. 2018, *MNRAS*, 473, 603